ChemPubSoc Europe

DOI: 10.1002/open.201800259

Open Access ChemistryOPEN Full Papers

Special Collection

Mechanistic Insights into a Stibene Cleavage Oxygenase NOV1 from Quantum Mechanical/Molecular Mechanical Calculations

Jiarui Lu and Wenzhen Lai*[a]

NOV1, a stilbene cleavage oxygenase, catalyzes the cleavage of the central double bond of stilbenes to two phenolic aldehydes, using a 4-His Fe(II) center and dioxygen. Herein, we use in-protein quantum mechanical/molecular mechanical (QM/MM) calculations to elucidate the reaction mechanism of the central double bond cleavage of phytoalexin resveratrol by NOV1. Our results showed that the oxygen molecule prefers to bind to the iron center in a side-on fashion, as suggested from the experiment. The quintet Fe–O_2 complex with the side-on superoxo antiferromagnetic coupled to the resveratrol radical is identified as the reactive oxygen species. The QM/MM results support the dioxygenase mechanism involving a dioxetane intermediate with a rate-limiting barrier of 10.0 kcal mol^{-1}. The alternative pathway through an epoxide intermediate is ruled out due to a larger rate-limiting barrier (26.8 kcal mol^{-1}). These findings provide important insight into the catalytic mechanism of carotenoid cleavage oxygenases and also the dioxygen activation of non-heme enzymes.

1. Introduction

Resveratrol, 3,5,4′-trihydroxy-*trans*-stilbene, is a phytoalexin produced by several spermatophytes in response to injury or pathogens attack.[1] It has attracted much attention due to its anti-aging and cardioprotective powers. However, it is still unclear how this phenolic compound is metabolized and what other effects it may have on the human body.

Resveratrol belongs to the stilbene family, which are diphenyl ethene compounds produced naturally in various plants and some bacteria. So far, four enzymes, NOV1 and NOV2 from *Novosphingobium aromaticivorans*,[2] Rco1 from *Ustilago maydis*,[3] and CAO1 from *Neurosporacrassa*[4] were identified as resveratrol cleavage enzymes that catalyze the oxidative cleavage of resveratrol at the interphenyl double bond, forming two phenolic aldehydes. Together with lignostilbene α,β-dioxygenase (LSD) from *Sphingomonas paucimobilis*,[5] these enzymes are recently classified as the members of stibene cleavage oxygenases (SCOs), which catalyze the double bond cleavage of stilbenes.[6] SCOs are related to carotenoid cleavage oxygenases (CCOs), which are non-heme Fe(II)-dependent enzymes that catalyze oxidative cleavage of double bonds in the conjugated carbon chain of carotenoids by dioxygen. In some literatures,[7–9] SCOs were also called as stilbenoid-cleaving CCOs.

For CCOs (including SCOs), the central question about the reaction mechanism is whether one or two oxygen atoms of molecular oxygen is/are incorporated into the products. Although a number of studies using isotopically labeled O_2 and H_2O were carried out to address this question, the issue is still under debate. Both monooxygenase and dioxygenase mechanisms have been proposed (Scheme 1). In the dioxygenase route, dioxygen adds to the double bond forming a dioxetane intermediate, which undergoes fragmentation to afford the products. Clearly, it requires the incorporation of both oxygen atoms from molecular oxygen into the aldehyde products. Several studies on reaction mechanism of *Arabidopsis* CCD1[10–12] suggested that the oxidative cleavage of substrate was catalyzed via a dioxygenase mechanism. On the other hand, the monooxygenase mechanism involves an Fe(IV)=O species with the formation of an epoxide intermediate. Then, the epoxide reacts with water generating a diol intermediate, which is finally oxidative cleaved to two aldehyde products. In this case, the products of the enzymatic reaction should contain equal quantities of oxygen derived from O_2 and H_2O. Studies on chicken β-carotene 15,15′-oxygenase (BCO1),[13] NOV2,[2] isoeugenol monooxygenase (Iem) from *Pseudomonas nitroreducens* Jin1[14] suggested a monooxygenase pattern of oxygen incorporation. It seems that both monooxygenase and dioxygenase mechanisms may exist within the CCO enzyme family. Theoretically, density functional theory (DFT) study of apocarotenoid oxygenase (ACO), a prototypical carotenoid-cleaving CCO, suggested that both monooxygenase and dioxygenase mechanisms are feasible.[15] However, recent studies on human BCO1,[16] *Synechocystis* ACO and *Novosphingobium* NOV2[9] using improved assay systems suggested that they are dioxygenases rather than monooxygenases as previously thought. As such,

[a] J. Lu, Dr. W. Lai
Department of Chemistry
Renmin University of China
No. 59 Zhongguancun Street, Haidian District Beijing, 100872, P. R. China
E-mail: wenzhenlai@ruc.edu.cn

Supporting information for this article is available on the WWW under https://doi.org/10.1002/open.201800259

An invited contribution to a Special Collection dedicated to Computational Chemistry

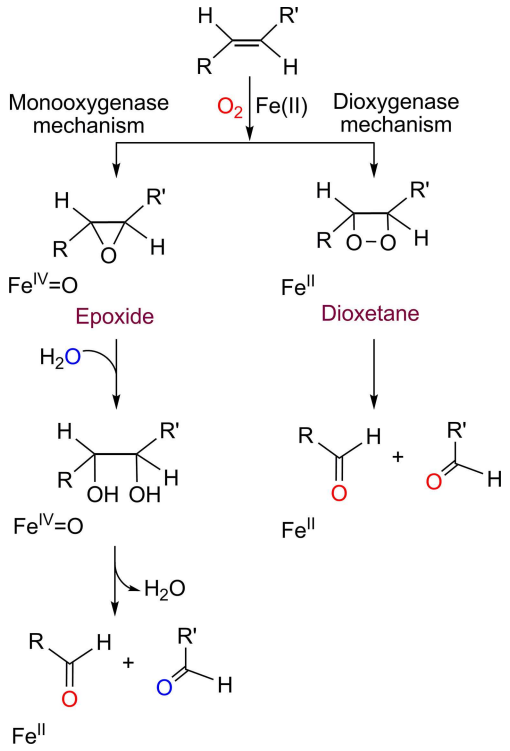

Scheme 1. Two Proposed Mechanisms for Oxidative Cleavage with CCOs.

Kiser *et al.* hold that dioxygenase activity is a feature common among the enzyme family.[9]

The geometric and electronic structures of the Fe–O_2 complex have attracted great interest in the non-heme iron enzymes and their biomimetic compounds since it is the first oxygen species during the dioxygen activation and could act as an active oxidant. Recently, a breakthrough for resveratrol cleavage enzymes has been made on the crystallographic structure of NOV1.[6] Like CCOs, the non-heme iron center of NOV1 is coordinated by four histidine ligands. More importantly, the structure of NOV1 in complex with dioxygen and substrate showed that the oxygen molecule bind to the iron in a side-on fashion. Moreover, the authors claimed that no waters are observed in coordination with the iron or anywhere proximal to substrate. A study of Viviparous14 (VP14), a CCO that is responsible for the oxidative cleavage of 11,12 double bond of 9-*cis*-epoxycarotenoid, however, showed that dioxygen bound to iron in an end-on fashion.[17] In addition, one water molecule was found to be coordinated to the iron, forming a six-coordinate ferrous site of VP14. Hence, the CCO Fe–O_2 complex remains poorly characterized from an experimental standpoint.[8] Note that the side-on binding of the molecular oxygen to the mononuclear iron center has been identified in naphthalene dioxygenase (NDO)[18] and homo-protocatechuate 2,3-dioxygenase (HPCD).[19] Note also that the dioxygen adduct of VP14 is in the absent of substrate. It is possible that the binding of substrate could affect the manner of dioxygen binding. Carbazole 1,9a-dioxygenase (a rieske nonheme iron oxygenase), for example, have shown that substrate binding regulates the manner of dioxygen binding in a side-on fashion.[20] A recent crystallographic study of a SCO from CAO1 showed that the iron center is a five-coordinate with a water ligand in the resting state.[7] It is expected that the water ligand will be displaced upon dioxygen binding. As such, we feel that the X-ray structure of NOV1 in complex with substrate and dioxygen is a good starting point to investigate the mechanism of CCOs.

In the present study, quantum mechanical/molecular mechanical (QM/MM) calculations have been carried out to elucidate the reaction mechanism of resveratrol cleavage by NOV1. As should be demonstrated, the oxygen molecule prefers to bind to the iron center in a side-on fashion in NOV1, as suggested from the experiment.[6] The quintet Fe–O_2 complex with the side-on superoxo antiferromagnetic coupled to the resveratrol radical is the reactive oxygen species. Our results support the dioxygenase mechanism involving a dioxetane intermediate. The alternative pathway via an epoxide intermediate was ruled out due to a much larger rate-limiting barrier.

2. Results and Discussion

2.1. Dioxygen Binding to the Iron

In the present study, we first computed the Fe–O_2 complexes in the singlet, triplet, quintet, and septet spin states. Table 1 gives relative energies of these four spin states. Figure 1 displays the QM/MM-optimized geometries of the Fe–O_2 complexes along with most interesting bond lengths and spin densities. For the septet and quintet states, both side-on and end-on conformations were located, while for the triplet and singlet states, only side-on conformation was obtained. We found that the dioxygen molecule prefers to bind to the iron in a side-on mode as suggested from the experiment.[6] Most theoretical studies on the nonheme iron enzymes predicted a high spin septet ground state for the Fe–O_2 complex.[21–39] Here too, the septet state with the side-on conformation ($^7\mathbf{1}_{\text{side-on}}$ in Figure 1A) was found to be the most stable one, and then was set as the reference point of 0 kcal mol^{-1}. To better understand the electronic structure, analysis of the spin natural orbitals (SNOs) were also performed for the Fe–O_2 complexes. Below, we will

Table 1. Relative Energies (in kcal mol^{-1})[a] of the septet, quintet, triplet, and singlet states of the Fe-O_2 complex.

Species	ΔE(B3LYP)	ΔE(B3LYP-D3)	ΔE(B3LYP-D3) + ZPE
$^7\mathbf{1}_{\text{side-on}}$	0.0	0.0	0.0
$^7\mathbf{1}_{\text{end-on}}$	4.0	4.9	14.9
$^5\mathbf{1}_{\text{side-on}}$	1.0	1.5	8.5
$^5\mathbf{1}_{\text{end-on}}$	15.1	14.0	16.3
$^3\mathbf{1}_{\text{side-on}}$	2.3	2.7	11.2
$^3\mathbf{1}'_{\text{side-on}}$	1.4	2.0	11.2
$^1\mathbf{1}_{\text{side-on}}$	1.8	1.8	4.8

[a] Relative energies ΔE(B3LYP) were obtained from single-point calculation at the QM(B3LYP/B2)/MM level. Energies ΔE(B3LYP-D3) and ΔE(B3LYP-D3) + ZPE were obtained by including the dispersion correction, and both dispersion and ZPE corrections, respectively.

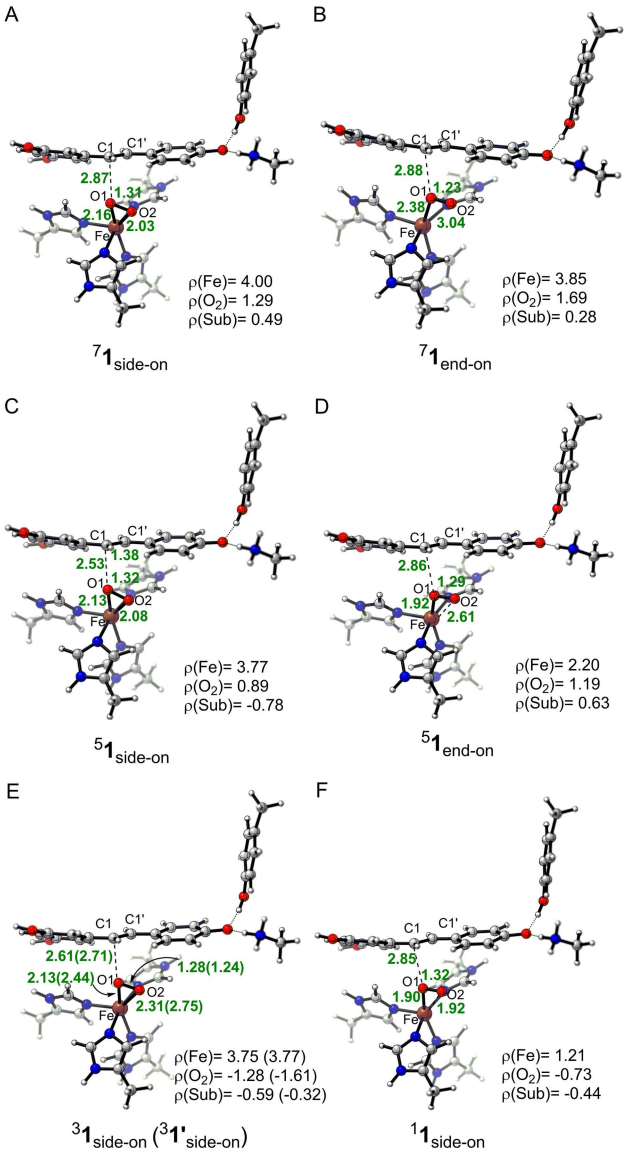

Figure 1. QM/MM-optimized structures of the Fe–O_2 complex **1**. A) $^{7}\mathbf{1}_{side\text{-}on}$; B) $^{7}\mathbf{1}_{end\text{-}on}$; C) $^{5}\mathbf{1}_{side\text{-}on}$; D) $^{5}\mathbf{1}_{end\text{-}on}$; E) $^{3}\mathbf{1}_{side\text{-}on}$ and $^{3}\mathbf{1'}_{side\text{-}on}$; F) $^{1}\mathbf{1}_{side\text{-}on}$. Distances are given in Å.

discuss the geometric and electronic characters of all the located Fe–O_2 complexes as well as their relative energies in detail.

Septet States

For the septet spin state, the side-on conformation ($^{7}\mathbf{1}_{side\text{-}on}$) is characterized by two Fe–O distances of 2.16 Å and 2.03 Å. The O–O bond length is of 1.31 Å, indicating a superoxo character of the dioxygen ligand. The spin densities on Fe, O_2, and resveratrol (Res) in $^{7}\mathbf{1}_{side\text{-}on}$ are 4.0, 1.29, and 0.49, respectively. It suggested that partial electron transfer occurs from substrate to dioxygen. Analysis of the spin natural orbitals (Figure S4 in the SI) revealed that the electronic structure of this septet state is best described as a mixture of two reference configurations. One of the reference configurations should have an Fe(II) and a triplet dioxygen. The second reference configuration should have an Fe(II) but a superoxide radical and a resveratrol radical, with all spins parallel. Compared with the side-on conformation, the end-on one ($^{7}\mathbf{1}_{end\text{-}on}$ in Figure 1B) has longer Fe-oxygen bond distances of 2.38 Å and 3.04 Å, and shorter O–O bond length of 1.23 Å. The spin densities on Fe, O_2, and Res are 3.85, 1.69, 0.28, respectively, implying that $^{7}\mathbf{1}_{end\text{-}on}$ is mainly a high-spin Fe(II) complex with a triplet dioxygen. $^{7}\mathbf{1}_{end\text{-}on}$ lies 4.9 kcal mol^{-1} higher than the side-on one at the QM(B3LYP-D3)/MM level. The zero-point energy (ZPE) correction increases the energy gap to 14.9 kcal mol^{-1}.

Quintet States

For the quintet state, the side-on one ($^{5}\mathbf{1}_{side\text{-}on}$ in Figure 1C) has two Fe–O bond lengths of 2.13 and 2.08 Å. The spin densities on iron, dioxygen, and Res are 3.77, 0.89, and −0.78, respectively. Thus, $^{5}\mathbf{1}_{side\text{-}on}$ has six unpaired electrons and its electronic structure can be described as a high-spin Fe(II) complex with a superoxo and a resveratrol radical (see the SNOs in Figure S6). The antiparallel spin of the unpaired electrons on substrate and dioxygen will be suited for formation of a bond between the two radicals. Energetically, $^{5}\mathbf{1}_{side\text{-}on}$ is only 1.5 kcal mol^{-1} higher than $^{7}\mathbf{1}_{side\text{-}on}$ without ZPE correction. After including the ZPE correction, the energy gap increases to 8.5 kcal mol^{-1}.

In the end-on one, $^{5}\mathbf{1}_{end\text{-}on}$ (Figure 1D), the spin densities on iron, dioxygen, and Res are 2.20, 1.19, and 0.63, respectively. Analysis of SNOs (Figure S7) demonstrated that $^{5}\mathbf{1}_{end\text{-}on}$ has four unpaired electrons. It is an intermediate-spin Fe(II) with a superoxo radical and a resveratrol radical, with all spins parallel. The calculated relative energy of $^{5}\mathbf{1}_{end\text{-}on}$ is 16.3 kcal mol^{-1}, compared to $^{7}\mathbf{1}_{side\text{-}on}$ at the B3LYP-D3/MM level with ZPE correction. Note that all attempts to locate the end-on Fe–O_2 complex having the same electronic structure as $^{5}\mathbf{1}_{side\text{-}on}$ failed as they always result in a side-on complex.

Triplet States

It can be seen from Table 1, the energies of two triplet states are very close, both lie 11.2 kcal mol^{-1} (ΔE(B3LYP-D3) + ZPE) above $^{7}\mathbf{1}_{side\text{-}on}$. For $^{3}\mathbf{1}_{side\text{-}on}$ (Figure 1E), the spins on the half-oxidized and half-reduced species are antiferromagnetically coupled with that on the iron. Compared with $^{3}\mathbf{1}_{side\text{-}on}$, $^{3}\mathbf{1'}_{side\text{-}on}$ has longer Fe–O bond lengths of 2.44 and 2.75 Å, suggesting a weak dioxygen bonding interaction. In $^{3}\mathbf{1'}_{side\text{-}on}$, the spin densities on iron, dioxygen and resveratrol are 3.77, −1.61, and −0.32, respectively. Analysis of SNOs (see Figure S9) suggested that $^{3}\mathbf{1'}_{side\text{-}on}$ is mainly a high-spin Fe(II) complex with a triplet dioxygen.

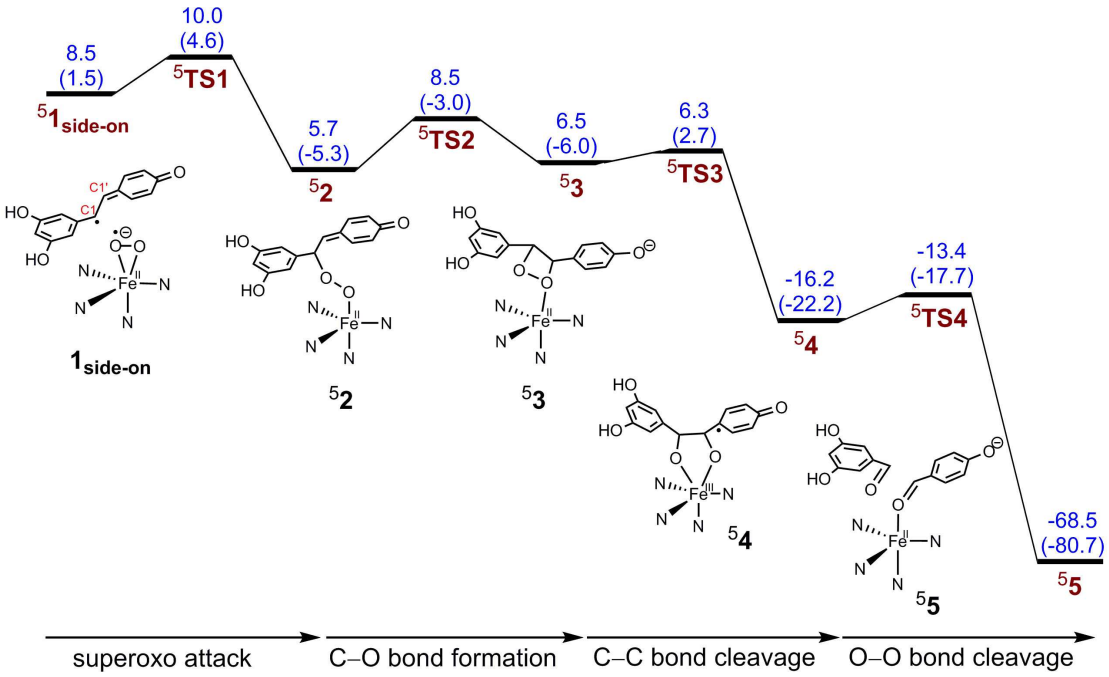

Figure 2. Calculated energy profile for the dioxetane mechanism. The values in or outside parentheses are QM(B3LYP-D3)/MM energies (in kcal mol^{-1}) without or with ZPE corrections.

Singlet States

As shown in Figure 1F, $^{1}\mathbf{1}_{side\text{-}on}$ has two Fe–O bond lengths of 1.90 and 1.92 Å. The spin densities on iron, dioxygen and resveratrol are 1.21, −0.73, and −0.44, respectively. Similar with $^{7}\mathbf{1}_{side\text{-}on}$, $^{1}\mathbf{1}_{side\text{-}on}$ can be described as being between the two limiting cases, Fe^{II}–O_2 and Fe^{II}–$O_2^{\bullet-}$. The calculated relative energy of $^{1}\mathbf{1}_{end\text{-}on}$ is 4.8 kcal mol^{-1} (ΔE(B3LYP-D3) + ZPE) compared to $^{7}\mathbf{1}_{side\text{-}on}$.

2.2. Reaction Mechanism

In all the located Fe–O_2 complexes, only $^{5}\mathbf{1}_{side\text{-}on}$ has antiparallel spin of the unpaired electrons on substrate and dioxygen, which will facilitate formation of a bond between the two radicals. It has been extensively showed by theoretical studies that in many mononuclear non-heme enzymes the quintet Fe–O_2 is the reactive species.[15,29,30,33,35,38-48] As such, we took $^{5}\mathbf{1}_{side\text{-}on}$ as the catalytically relevant state for the oxidative cleavage of resveratrol. The subsequent QM/MM calculations were carried out on the quintet surface. Two possible pathways, namely, dioxetane mechanism and epoxide mechanism, were found to be both feasible in a DFT study of ACO.[15] Therefore, these two pathways were investigated here for NOV1. Unless otherwise stated, the QM(B3LYP-D3)/MM energies with ZPE corrections were mentioned.

Mechanism A: Dioxetane Mechanism

We first consider the previous proposed dioxygenase route via a dioxetane intermediate. The calculated energy profile is then given in Figure 2. A detailed discussion of the mechanism is present below.

From the inspection of Figure 1, we note that the dioxygen is positioned close to the C1=C1′ double bond of substrate. Especially, the distance between O1 and C1 is 2.53 Å in $^{5}\mathbf{1}_{side\text{-}on}$, which is much shorter than the distance between O2 and C1′ (3.36 Å). As such, the most straightforward reaction is the attack of O1 of the superoxide on the substrate C1. The structure of the fully optimized transition state (^{5}**TS1**) for this process is displayed in Figure 3A, in which the nascent O1–C1 bond is decreased to 1.91 Å. The spin decreased from −0.78 to −0.50 for Res and from 0.89 to 0.54 for dioxygen. The energy of ^{5}**TS1**

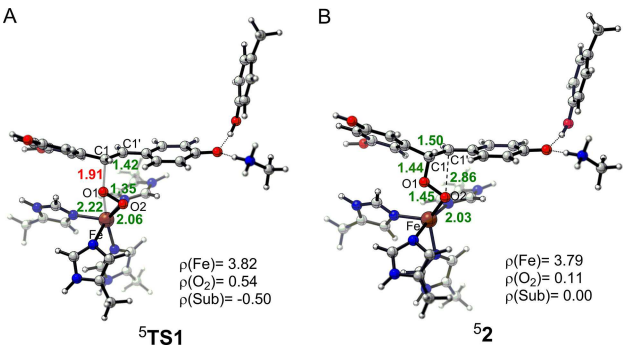

Figure 3. Optimized structures for TS and product in the first step of reaction. A) ^{5}**TS1**; B) ^{5}**2**. Distances are given in Å.

lies 1.5 kcal mol^{-1} above ^{5}**1**$_{side\text{-}on}$, and is 10.0 kcal mol^{-1} higher than ^{7}**1**$_{side\text{-}on}$. The so-generated intermediate ^{5}**2** (Figure 3B), lying 2.8 kcal mol^{-1} below ^{5}**1**$_{side\text{-}on}$. Spin on Res and O_2 is 0.00 and 0.11, respectively, suggesting the electron transfer from substrate to dioxygen completes. And the C1–C1′ bond length increases from 1.38 Å to 1.50 Å, whereas the O–O bond length increases from 1.32 Å to 1.45 Å. Clearly, ^{5}**2** is a peroxo-bridged intermediate.

During the conversion from ^{5}**1**$_{side\text{-}on}$ to ^{5}**2**, the distance between the proximal oxygen (O2) and substrate C1′ is decreased from 3.36 Å to 2.86 Å. The next step involves the second O–C (O2–C1′) bond formation leading to a dioxetane intermediate. During this process, the O2–C1′ distance is decreased to 2.24 Å in ^{5}**TS2** (Figure 4A) and to 1.54 Å in the dioxetane intermediate ^{5}**3** (Figure 4B). The calculated reaction barrier for this step is 2.8 kcal mol^{-1}.

In ^{5}**3** (Figure 4B), one oxygen atom of the dioxetane group (O2) is in contact with the iron center with a distance of 2.20 Å. It has been proposed by Borowski *et al.* in their DFT study of ACO[15] that this Fe–O contact will facilitates the O–O bond cleavage of dioxetane. We found here that the O–O bond cleavage of the dioxetane intermediate is coupled with the Fe–O1 bond formation. In the transition state for this step (^{5}**TS3** in Figure 5A), the O–O bond length is 1.78 Å, whereas the Fe–O1 distance is decreased to 3.24 Å. In the product of this step, ^{5}**4** (Figure 5B), the deprotonated diol is coordinated to the iron through two oxygen atoms originated from dioxygen. Spin population analysis suggested that it is an Fe^{III} species antiferromagnetically coupled with a diolate radical. Further SNOs analysis showed that the spin on the substrate is mainly delocalized on the O-benzyl group (Figure 6). The calculated barrier for this step is 8.7 kcal mol^{-1} without ZPE correction. After applying the ZPE correction, the barrier decreases to 0.2 kcal mol^{-1}. The so-generated ^{5}**4** (Figure 5B) is 22.7 kcal mol^{-1} lower than ^{5}**3**.

Finally, the C–C bond cleavage is accompanied by an electron transfer from the diol radical to iron, yielding two aldehyde products. At the optimized TS of this step (^{5}**TS4** in Figure 7A), the C–C bond length amounts to 1.87 Å. The spin on the diol is −0.68 in ^{5}**TS4**, which is only slightly lower than that (−0.76) in ^{5}**4**. Therefore, the electron transfer occurs after transit through the TS. In the final product ^{5}**5** (Figure 7B), 4-hydroxybenzaldehyde (in its deprotonated form) is bound to the iron. This step has a barrier of 2.8 kcal mol^{-1} and an exothermicity of 52.3 kcal mol^{-1}.

It can be seen from the calculated energy profile for the mechanism A (Figure 2) that the first step, i.e., the superoxide attack on the substrate, is the rate-limiting step with a total barrier of 10.0 kcal mol^{-1}. During this attack, a spin crossing from the septet state to the quintet state is needed, since the Fe–O_2 complex has a septet ground state.

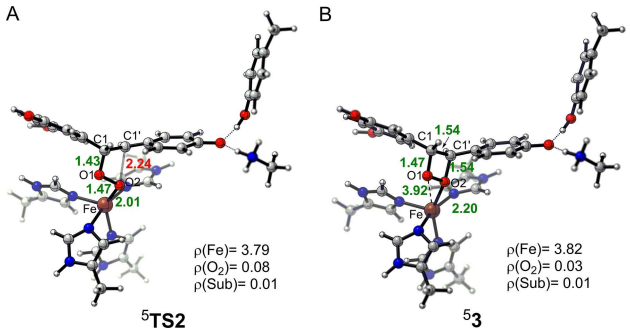

Figure 4. Optimized structures for A) ^{5}**TS2** and B) ^{5}**3**. Distances are given in Å.

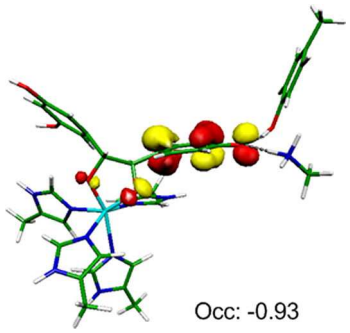

Figure 6. Spin natural orbital with negative occupancy number (Occ) in ^{5}**4**.

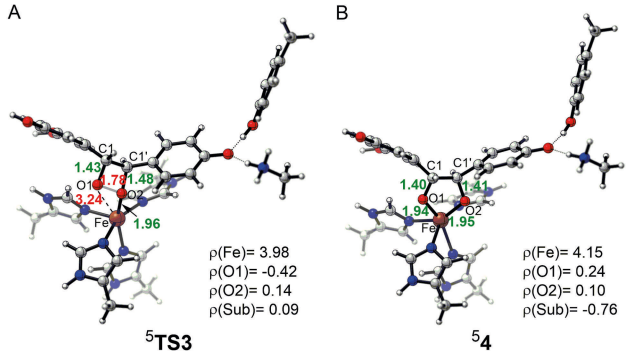

Figure 5. Optimized structures of TS and product in the O–O bond cleavage of the dioxetane intermediate. A) ^{5}**TS3**; B) ^{5}**4**. Distances are given in Å.

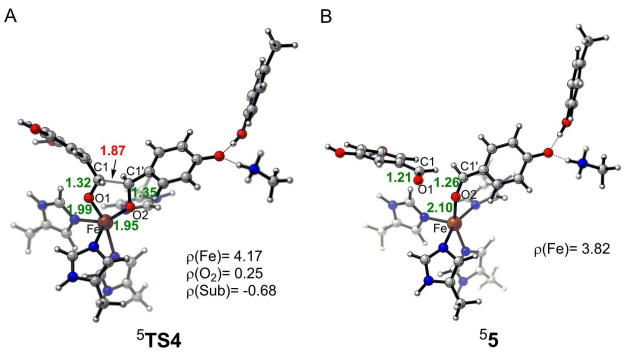

Figure 7. Optimized structures of TS and product for the final C–C bond cleavage. A) ^{5}**TS4**; B) ^{5}**5**. Distances are given in Å.

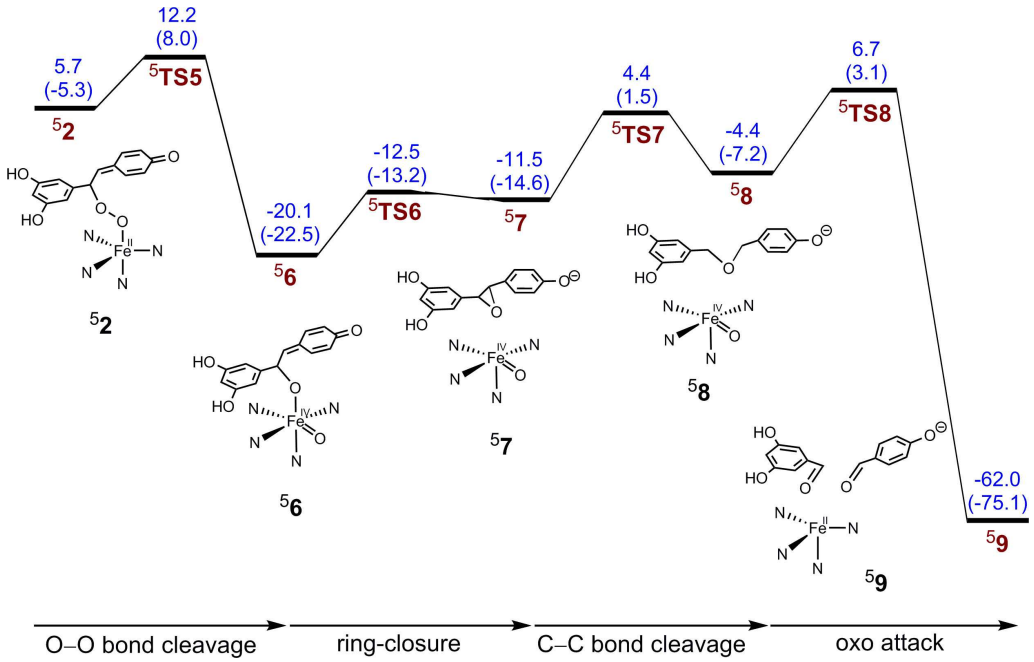

Figure 8. Calculated energy profile for the epoxide mechanism. The relative energies given in kcal mol^{-1} at the QM(B3LYP-D3/B2)/MM levels of theory. The values in or outside parentheses are energies without or with ZPE corrections.

Mechanism B: Epoxide Mechanism

A previous DFT study for ACO showed that the dioxygenase-labeling pattern could be achieved through either dioxetane or epoxide intermediates.[15] In their study, the attack of the end-on Fe^{II}-superoxo complex (without water ligand) on the substrate radical gives an epoxide intermediate directly. However, this end-on species was not found here in NOV1. As already mentioned above, the attack of the reactive Fe–O_2 complex (having side-on binding mode) on the substrate generates a peroxo-bridged species. Interesting to note that the peroxo-bridged species has been trapped in an aromatic ring cleavage enzyme, homoprotocatechuate 2,3-dioxygenase (HPCD).[19] It can undergo O–O bond cleavage followed by O–C bond formation to afford an epoxide.[33,35, 36, 49] Furthermore, the ring-opening of epoxide followed by attack of the Fe-bound oxygen can form aldehydes. We then examined the possibility of involving the epoxide intermediate in the cleavage reaction of resveratrol by NOV1 starting from the peroxo-bridged species.

The calculated energy profile was shown in Figure 8. As expected, the O–O bond cleavage of the peroxo-bridged species followed by ring-closure gives the epoxide intermediate (^{5}**7**). The opening of the epoxide ring followed by the attack of the oxo atom (accompanied by the C–O bond breaking) yields two aldehyde products. In the final product ^{5}**9**, the dihydroxy product, 3,5-dihydroxybenzaldehyde, is bound to the iron. However, the O–O bond cleavage of the peroxo-bridged species was found to have a barrier of 6.5 kcal mol^{-1}, which is 3.7 kcal mol^{-1} higher than the dioxetane formation (^{5}**TS2** in Figure 2). As such, the O–O bond cleavage is kinetically disfavored. Moreover, the generated Fe^{IV}=O species, ^{5}**6**, is very stable, being 26.6 kcal mol^{-1} lower than the dioxetane intermediate (^{5}**3**). It can be seen from Figure 8 that the rate-limiting barrier for epoxide mechanism is 26.8 kcal mol^{-1}, being much higher than that for dioxetane mechanism (10.0 kcal mol^{-1}). Based on these findings, the epoxide mechanism can be ruled out.

3. Conclusions

To fully understand the reaction mechanism of resveratrol cleavage by NOV1, the QM/MM calculations were carried out. The results showed that the oxygen molecule prefers to bind to the iron center in a side-on fashion, as suggested from the experiment.[6] The quintet Fe–O_2 complex with the side-on superoxo antiferromagnetic coupled to the resveratrol radical (^{5}**1**$_{side\text{-}on}$) was found to be the reactive oxygen species. The high-energy pathway involving an epoxide intermediate is ruled out. The mechanism of resveratrol cleavage catalyzed by NOV1 involves an attack of superoxo on C1, followed by second C–O bond formation leading to the dioxetane intermediate. The subsequent O–O bond cleavage generates a diol radical complex. Finally, the C–C bond cleavage coupled with electron transfer from the diol radical to iron gives two aldehyde products.

Methods

Setup of the System

The initial structure was taken from the crystal structure of NOV1 in complexed with dioxygen and resveratrol (PDB code: 5j54).[6] All missing hydrogen atoms were added via the HBUILD[50] module and optimized by using the CHARMM force field as implemented in the CHARMM program.[51] The resulting protein was then solvated with a 16 Å-thick water solvent layer followed by energy minimization at the MM level using CHARMM force field to attain equilibrium of the inner solvent layer. A productive molecular dynamics (MD) run was performed. During the MD simulations, the coordinates of the iron-dioxygen unit and the metal-ligating residues as well as the outer 8 Å of the solvent layer were kept fixed.

Protonation States

The protonation states of all the titratable residues were determined by the combination of the pK_a values estimated by the PROPKA[52] program and careful visual inspection of local hydrogen-bond networks. Among the histidine residues, His28, His69, His167 and His218, His230, His247, His257, His284, His296, His314, His326, His368, His397, His476 were protonated at the δ position, whereas His71 and His407 are doubly protonated. Based on the calculated pK_a values, all glutamate (Glu) and aspartate (Asp) residues were treated as deprotonated, while all arginines (Arg) and lysines (Lys) residues were positively charged. It can be noted that for NOV1, the 4′-OH group of the resveratrol substrate forms two hydrogen bonds to the side-chain hydroxyl group of Tyr101 and the N-terminus tail of Lys135, thus lowing the pK_a value of resveratrol (associated with the deprotonation of the phenol group, 4′-OH) to 7.2. As such, the protonated and deprotonated forms of 4′-OH are both possible. However, the MD simulation for the Fe-dioxygen complex with the protonated substrate showed that Tyr101 and Lys134 residues move away from the substrate after 3.3 ns (see Figures S1 in the SI). Instead, when the deprotonated form of substrate was used, these two residues, Tyr101 and Lys134, are still within hydrogen bond distance of the substrate (Figure S2). Thus, the deprotonated form of resveratrol was used in the following QM/MM calculations. In addition, the root mean square deviation (RMSD) of the backbone atoms of the protein reveals that the system using the deprotonated substrate has reached equilibrium after 1 ns (see Figure S3 in the SI). A random snapshot from the equilibrium MD trajectory was used as a starting point for the subsequent QM/MM calculations.

QM/MM Methodology

All the QM/MM calculations were performed with the ChemShell package[53] which combining the Turbomole[54] for the QM part and DL_POLY[55] for the MM part. An electronic embedding scheme[56] was applied to include the polarizing effect of the enzymatic environment on the QM region. Hydrogen link atoms[57] with the charge shift model were used to treat the QM/MM boundary. The QM region comprises of the resveratrol, iron-dioxygen, the methylimidazole group of histidines, His167, His218, His284, and His476, phenol for Tyr101, and CH_3NH_3 for Lys134.

The QM part was treated by density functional theory (DFT) with the hybrid B3LYP[58,59] functional, while the MM part was handled with the CHARMM force field. Geometry optimization and frequency calculations were performed with def-SV(P) (labelled as B1). The energies were corrected by single-point calculations using a larger all-electron basis set B2, which is def2-TZVP for all the atoms. The transition states (TSs) were located by initial potential energy surface scans followed by full TS optimizations using the partitioned rational function optimization (P-RFO) algorithm implemented in the HDLC code.[60] The QM/MM frequency calculations were performed for QM atoms in the present of MM atoms to characterize the nature of the stationary points and to determine the zero-point energy (ZPE). The empirical dispersion correction was further calculated by using the Grimme's DFT-D3 program.[61] Here, the ZPE correction was found to have larger effect on the relative energies. Then the energies with and without ZPE correction were both given in the present study.

Acknowledgements

The work is supported by the National Natural Science Foundation of China (No. 21673286), the Fundamental Research Funds for the Central Universities, the Research Funds of Renmin University of China (program No. 16XNLQ04), and High-performance Computing Platform of Renmin University of China.

Conflict of Interest

The authors declare no conflict of interest.

Keywords: non-heme · carotenoid cleavage oxygenases · QM/MM · reaction mechanism · resveratrol

[1] L. Fremont, *Life Sci.* **2000**, *66*, 663–673.
[2] E. K. Marasco, C. Schmidt-Dannert *ChemBioChem.* **2008**, *9*, 1450–1461.
[3] T. Brefort, D. Scherzinger, M. Limon, A. F. Estrada, D. Trautmann, C. Mengel, J. Avalos, S. Al-Babili, *Fungal Genet. Biol.* **2011**, *48*, 132–143.
[4] V. Diaz-Sanchez, A. F. Estrada, M. C. Limon, S. Al-Babili, J. Avalos, *Eukaryotic Cell* **2013**, *12*, 1305–1314.
[5] S. Kamoda, Y. Saburi, *Biosci. Biotechnol. Biochem.* **1993**, *57*, 931–934.
[6] R. P. McAndrew, N. Sathitsuksanoh, M. M. Mbughuni, R. A. Heins, J. H. Pereira, A. George, K. L. Sale, B. G. Fox, B. A. Simmons, P. D. Adams, *Proc. Natl. Acad. Sci. USA* **2016**, *113*, 14324–14329.
[7] X. Sui, A. C. Weitz, E. R. Farquhar, M. Badiee, S. Banerjee, J. von Lintig, G. P. Tochtrop, K. Palczewski, M. P. Hendrich, P. D. Kiser, *Biochemistry* **2017**, *56*, 2836–2852.
[8] X. Sui, E. R. Farquhar, H. E. Hill, J. von Lintig, W. Shi, P. D. Kiser, *J. Biol. Inorg. Chem.* **2018**, *23*, 887–901.
[9] X. W. Sui, M. Golczak, J. Y. Zhang, K. A. Kleinberg, J. von Lintig, K. Palczewski, P. D. Kiser, *J. Biol. Chem.* **2015**, *290*, 30212–30223.
[10] R. A. Creelman, J. A. D. Zeevaart, *Plant Physiol.* **1984**, *75*, 166–169.
[11] J. A. D. Zeevaart, T. G. Heath, D. A. Gage, *Plant Physiol.* **1989**, *91*, 1594–1601.
[12] H. Schmidt, R. Kurtzer, W. Eisenreich, W. Schwab, *J. Biol. Chem.* **2006**, *281*, 9845–9851.
[13] M. G. Leuenberger, C. Engeloch-Jarret, W. D. Woggon, *Angew. Chem. Int. Ed.* **2001**, *40*, 2614–2617.
[14] J. Y. Ryu, J. Seo, S. Park, J. H. Ahn, Y. Chong, M. J. Sadowsky, H. G. Hur *Biosci. Biotechnol. Biochem.* **2013**, *77*, 289–294.
[15] T. Borowski, M. R. A. Blomberg, P. E. M. Siegbahn, *Chem. Eur. J.* **2008**, *14*, 2264–2276.
[16] C. dela Sena, K. M. Riedl, S. Narayanasamy, R. W. Curley, S. J. Schwartz, E. H. Harrison, *J. Biol. Chem.* **2014**, *289*, 13661–13666.
[17] S. A. J. Messing, S. B. Gabelli, I. Echeverria, J. T. Vogel, J. C. Guan, B. C. Tan, H. J. Klee, D. R. McCarty, L. M. Amzel, *Plant Cell.* **2010**, *22*, 2970–2980.
[18] A. Karlsson, J. V. Parales, R. E. Parales, D. T. Gibson, H. Eklund, S. Ramaswamy, *Science* **2003**, *299*, 1039–1042.
[19] E. G. Kovaleva, J. D. Lipscomb, *Science* **2007**, *316*, 453–457.
[20] Y. Ashikawa, Z. Fujimoto, Y. Usami, K. Inoue, H. Noguchi, H. Yamane, H. Nojiri, *BMC Struct. Biol.* **2012**, *12*, 15.

[21] A. Bassan, M. R. A. Blomberg, P. E. M. Siegbahn, *Chem. Eur. J.* **2003**, *9*, 106–115.
[22] T. Borowski, A. Bassan, P. E. M. Siegbahn, *Biochemistry* **2004**, *43*, 12331–12342.
[23] T. Borowski, A. Bassan, P. E. M. Siegbahn, *Chem. Eur. J.* **2004**, *10*, 1031–1041.
[24] T. Borowski, V. Georgiev, P. E. M. Siegbahn, *J. Am. Chem. Soc.* **2005**, *127*, 17303–17314.
[25] A. Bassan, T. Borowski, C. J. Schofield, P. E. M. Siegbahn, *Chem. Eur. J.* **2006**, *12*, 8835–8846.
[26] A. V. Nemukhin, I. A. Topol, R. E. Cachau, S. K. Burt, *Theor. Chem. Acc.* **2006**, *115*, 348–353.
[27] G. Cicero, C. Carbonera, K. Valegard, J. Hajdu, I. Andersson, G. Ranghino, *Int. J. Quantum Chem.* **2007**, *107*, 1514–1522.
[28] S. Sinnecker, N. Svensen, E. W. Barr, S. Ye, J. M. Bollinger, F. Neese, C. Krebs, *J. Am. Chem. Soc.* **2007**, *129*, 6168–6179.
[29] H. Hirao, K. Morokuma, *J. Am. Chem. Soc.* **2010**, *132*, 17901–17909.
[30] H. Hirao, K. Morokuma, *J. Am. Chem. Soc.* **2011**, *133*, 14550–14553.
[31] H. Chen, W. Z. Lai, J. N. Yao, S. Shaik, *J. Chem. Theory Comput.* **2011**, *7*, 3049–3053.
[32] L. K. Du, J. Gao, Y. J. Liu, C. B. Liu, *J. Phys. Chem. B* **2012**, *116*, 11837–11844.
[33] G. J. Christian, S. F. Ye, F. Neese, *Chem. Sci.* **2012**, *3*, 1600–1611.
[34] A. Milaczewska, E. Broclawik, T. Borowski, *Chem. Eur. J.* **2013**, *19*, 770–780.
[35] G. Dong, S. Shaik, W. Z. Lai, *Chem. Sci.* **2013**, *4*, 3624–3635.
[36] G. Dong, W. Z. Lai, *J. Phys. Chem. B* **2014**, *118*, 1791–1798.
[37] A. Wójcik, M. Radoń, T. Borowski, *J. Phys. Chem. A* **2016**, *120*, 1261–1274.
[38] S. Roy, J. Kaestner, *Angew. Chem. Int. Ed.* **2016**, *55*, 1168–1172.
[39] X. D. Song, J. R. Lu, W. Z. Lai, *Phys. Chem. Chem. Phys.* **2017**, *19*, 20188–20197.
[40] P. E. M. Siegbahn, F. Haeffner, *J. Am. Chem. Soc.* **2004**, *126*, 8919–8932.
[41] V. Georgiev, T. Borowski, M. R. A. Blomberg, P. E. M. Siegbahn, *J. Biol. Inorg. Chem.* **2008**, *13*, 929–940.
[42] G. Dong, U. Ryde, *Inorg. Chem.* **2016**, *55*, 11727–11735.
[43] S. Roy, J. Kaestner, *Chem. Eur. J.* **2017**, *23*, 8949–8962.
[44] Y. Qi, J. R. Lu, W. Z. Lai, *J. Phys. Chem. B* **2016**, *120*, 4579–4590.
[45] A. S. Faponle, F. P. Seebeck, S. P. de Visser, *J. Am. Chem. Soc.* **2017**, *139*, 9259–9270.
[46] W. J. Wei, P. E. M. Siegbahn, R. Z. Liao, *Inorg. Chem.* **2017**, *56*, 3589–3599.
[47] Z. Wojdyla, T. Borowski, *J. Biol. Inorg. Chem.* **2018**, *23*, 795–808.
[48] Y. Li, X. Wang, R. Zhang, J. Wang, Z. Yang, L. Du, X. Tang, Q. Zhang, W. Wang, *ACS Earth Space Chem.* **2018**, *2*, 888–894.
[49] G. J. Christian, F. Neese, S. Ye, *Inorg. Chem.* **2016**, *55*, 3853–3864.
[50] A. T. Brunger, M. Karplus, *Proteins Struct. Funct. Genet.* **1988**, *4*, 148–156.
[51] A. D. MacKerell, D. Bashford, M. Bellott, R. L. Dunbrack, J. D. Evanseck, M. J. Field, S. Fischer, J. Gao, H. Guo, S. Ha, D. Joseph-McCarthy, L. Kuchnir, K. Kuczera, F. T. K. Lau, C. Mattos, S. Michnick, T. Ngo, D. T. Nguyen, B. Prodhom, W. E. Reiher, B. Roux, M. Schlenkrich, J. C. Smith, R. Stote, J. Straub, M. Watanabe, J. Wiorkiewicz-Kuczera, D. Yin, M. Karplus, *J. Phys. Chem. B* **1998**, *102*, 3586–3616.
[52] H. Li, A. D. Robertson, J. H. Jensen *Proteins Struct. Funct. Bioinf.* **2005**, *61*, 704–721.
[53] P. Sherwood, A. H. de Vries, M. F. Guest, G. Schreckenbach, C. R. A. Catlow, S. A. French, A. A. Sokol, S. T. Bromley, W. Thiel, A. J. Turner, S. Billeter, F. Terstegen, S. Thiel, J. Kendrick, S. C. Rogers, J. Casci, M. Watson, F. King, E. Karlsen, M. Sjovoll, A. Fahmi, A. Schafer, C. Lennartz, *J. Mol. Struct.* **2003**, *632*, 1–28.
[54] R. Ahlrichs, M. Bar, M. Haser, H. Horn, C. Kolmel, *Chem. Phys. Lett.* **1989**, *162*, 165–169.
[55] W. Smith, T. R. Forester, *J. Mol. Graphics* **1996**, *14*, 136–141.
[56] D. Bakowies, W. Thiel, *J. Phys. Chem.* **1996**, *100*, 10580–10594.
[57] A. H. de Vries, P. Sherwood, S. J. Collins, A. M. Rigby, M. Rigutto, G. J. Kramer *J. Phys. Chem. B* **1999**, *103*, 6133–6141.
[58] A. D. Becke *Phys. Rev. A* **1988**, *38*, 3098–3100.
[59] A. D. Becke *J. Chem. Phys.* **1993**, *98*, 5648–5652.
[60] S. R. Billeter, A. J. Turner, W. Thiel, *Phys. Chem. Chem. Phys.* **2000**, *2*, 2177–2186.
[61] S. Grimme, J. Antony, S. Ehrlich, H. Krieg, *J. Chem. Phys.* **2010**, *132*, 154104–154109.

Manuscript received: November 20, 2018
Revised manuscript received: January 30, 2019